High-Density, Conformable Conducting Polymer-Based Implantable Neural Probes for the Developing Brain

Liang Ma, Duncan J. Wisniewski, Claudia Cea, Dion Khodagholy,* and Jennifer N. Gelinas*

Neurologic and neuropsychiatric disorders substantially impact the pediatric population, but there is a lack of dedicated devices for monitoring the developing brain in animal models, leading to gaps in mechanistic understanding of how brain functions emerge and their disruption in disease states. Due to the small size, fragility, and high water content of immature neural tissue, as well as the absence of a hardened skull to mechanically support rigid devices, conventional neural interface devices are poorly suited to acquire brain signals without inducing damage. Here, the authors design conformable, implantable, conducting polymer-based probes (NeuroShanks) for precise targeting in the developing mouse brain without the need for skull-attached, rigid mechanical support structures. These probes enable the acquisition of high spatiotemporal resolution neurophysiologic activity from superficial and deep brain regions across unanesthetized behavioral states without causing tissue disruption or device failure. Once implanted, probes are mechanically stable and permit precise, stable signal monitoring at the level of the local field potential and individual action potentials. These results support the translational potential of such devices for clinically indicated neurophysiologic recording in pediatric patients. Additionally, the role of organic bioelectronics as an enabling technology to address questions in developmental neuroscience is revealed.

L. Ma, J. N. Gelinas
Department of Biomedical Engineering
Columbia University
New York, NY 10027, USA
E-mail: jng2146@cumc.columbia.edu
D. J. Wisniewski, C. Cea, D. Khodagholy, J. N. Gelinas
Department of Electrical Engineering
Columbia University
New York, NY 10027, USA
E-mail: dk2955@columbia.edu
J. N. Gelinas
Department of Neurology
Columbia University Irving Medical Center
New York, NY 10032, USA

1. Introduction

Monitoring neural network activity in the developing brain is critical to understanding how these networks become capable of supporting complex brain functions, as well as how their disruption can lead to pediatric neurologic and neuropsychiatric disorders.[1,2] This activity is comprised of dynamic neural oscillations in the local field potential (LFP) that organize the action potentials ("spikes") of individual neurons.[3–5] These oscillations are then coordinated across cell layers and brain regions, requiring advanced recording approaches to identify underlying mechanisms.[6–8]

As such, recording approaches that can sample the activity of a sufficient number of neurons so that different cell types and functions are represented at the temporal resolution of spike transmission are necessary.[9–11] Currently, only wire "tetrode" arrays[12] or silicon probes[13–17] have been used to acquire spike resolution data in the developing brains of animal models. Such approaches necessitate implantation and maintenance of a rigid structure within the small, fragile, immature brain, inducing substantial mechanical mismatch with the soft, high water-content tissue.[18] This mismatch results in the movement of electrodes relative to neurons, causing recording instability, increased potential for tissue damage, and risk of device failure.[19] Thus, these technologies have limited anatomical sampling and at times preclude the use of unanesthetized experimental set-ups, which are necessary to capture activity patterns related to waking brain functions and natural sleep. Additionally, current neural probes require fixation of the probe or its associated drive onto a hard surface such as a skull to allow targeting of the probe to brain structures. However, the immature calcification of the developing skull limits approaches that require probe fixation to the skull surface as it is not sufficiently rigid to resist mechanical deformation. Lastly, the lower Young's modulus of the developing brain due to its high water content results in the possibility of tissue movement relative to the skull and shear forces on any rigid, fixated implanted devices. Therefore, an optimal neural interface device should be soft and lightweight such that it can move with the brain without the need for an anchoring structure.
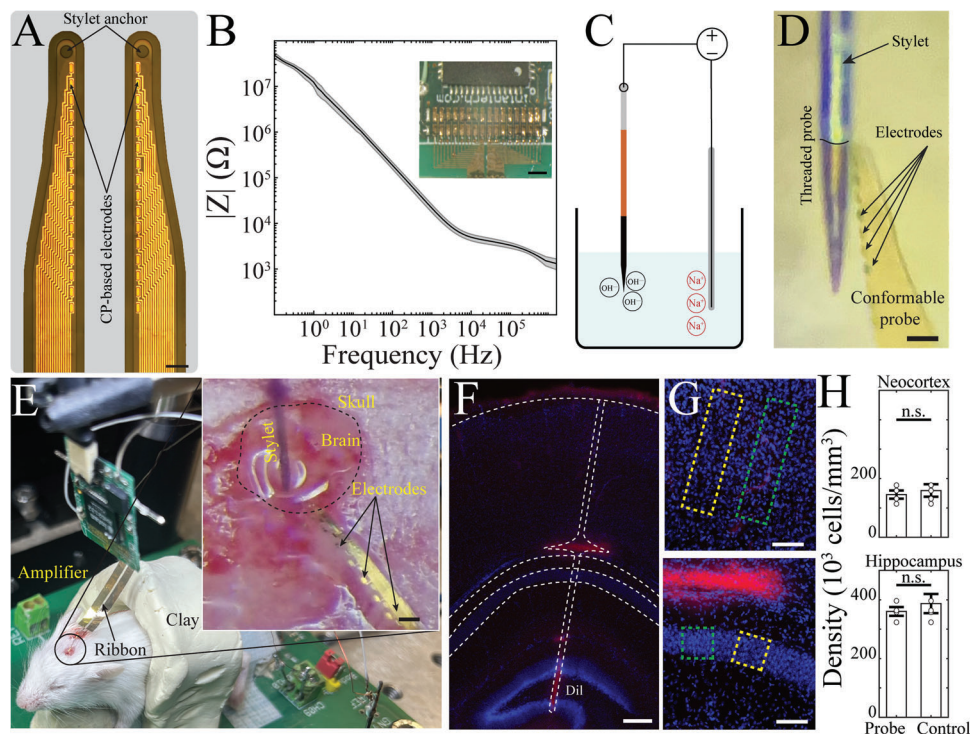
Figure 1. Device structure and implantation of NeuroShank with tungsten-based stylet. A) Micrograph of conformable probes with perforation used to attach stylet for implantation (scale bar, 30 µm). B) Electrochemical impedance spectroscopy of electrodes ($n = 32$ electrodes) across physiological bandwidth. Shaded area represents SEM. Inset: Micrograph of the back-end of the probe directly bonded to the acquisition electronics using mixed conducting particulate composites (scale bar, 1 mm). C) Simplified schematic of the electrochemical etching process of tungsten microwires using NaOH solution and direct current. D) Micrograph of a threaded probe and stylet (scale bar, 50 µm). E) Intra-operative image of a developing mouse skull (postnatal day 12). Inset: Craniotomy and one shank implanted with the other conforming to dura (scale bar, 100 µm). F) Fluorescence micrograph of a coronal slice of mouse pup brain processed with 4',-6diamidino--2phenylindole (DAPI) and vesicular glutamate transporter 2 (vGlut2) showing cortex, hippocampus, and NeuroShank implantation tract. The dashed lines highlight cortical and hippocampal layers as well as the location of the probe implantation marked by the diffused DiI marker (left, scale bar 200 µm). G) Fluorescence microscopy of the neocortex at implantation area (top; scale bar, 100 µm), and of the hippocampus at implantation area (bottom; scale bar, 100 µm). Green dashed boxes mark the stylet impacted area; yellow dashed boxes mark adjacent unimplanted areas serving as control tissue. H) Cell density quantification of tissue surrounding probe tract versus control tissue in the neocortex (top; $n = 4$ pups, paired t-test, $p = 0.1783$), and in hippocampal pyramidal cell layer (bottom; $n = 4$ pups, paired t-test, $p = 0.2035$).

The benefits of soft, miniaturized devices for pediatric applications have been well-recognized for epidermal and peripheral nerve applications.[20,21] Similar conformable substrates have been leveraged in adult animal models to record high spatiotemporal resolution neural activity using a variety of soft or stretchable materials.[22–31] Such devices can be coated with polyethylene glycol (PEG) to achieve temporary rigidity for implantation, but this process substantially increases the device diameter and thus the potential for adverse effects on surrounding tissue.[32,33] Although it is possible to eliminate the need for full diameter PEG insertion into the tissue by slow and gradual insertion of solely the dissolved section,[34] compatibility with short-duration surgery required in immature organisms and the ability to permit movement post-implantation remains unexplored. Furthermore, implanted probes are utilized in pediatric patients with medically refractory epilepsy to localize the epileptic network and guide therapeutic approaches, but rigid clinical electrodes designed for adult patients are currently employed.[35–37] Thus, despite the ongoing need, conformable technologies have not yet been investigated and evaluated for the acquisition of

high-quality LFP and neural spiking data from the developing brain.

Neural activity in immature neural networks is also different than that observed in mature networks, often with less precise spatiotemporal synchronization,[38–41] which can lead to signal detection challenges. Conducting polymers have lower electrochemical impedance than conventional metal electrodes due to their volumetric capacitance and mixed ionic-electronic conduction.[42–44] These properties increase electrode sensitivity, and concomitantly, the likelihood of identifying specific developmental patterns.[38] Poly(3,-4ethylenedioxythiophene) polystyrene sulfonate (PEDOT:PSS) in particular has been shown to enhance front-end acquisition capacity[31,45,46] and permit miniaturized, biocompatible integration with external silicon-based electronics.[47,48]

Here, we show that conformable shanks equipped with high-density conducting polymer-based microelectrodes (NeuroShanks) can reliably be implanted into various brain structures of the developing rodent using an easy-to-fabricate micronscale tungsten (W) stylet. We demonstrate that these conformable

**ADVANCED
SCIENCE NEWS**

www.advancedsciencenews.com

**ADVANCED
HEALTHCARE
MATERIALS**

www.advhealthmat.de

probes are mechanically robust to withstand the implantation process and the stylet can reliably and precisely target desired brain areas. We utilize the probes in unanesthetized mouse pups, permitting the recording of spontaneous neural activity across sleep and wake states without causing significant tissue disruption or device failure over the course of several hours. These probes enable the acquisition of high spatiotemporal resolution LFP, as well as action potentials that can be effectively clustered to identify activity patterns of individual neurons in the developing brain. Signals are stably maintained across the recording period, supporting a lack of probe movement relative to neural tissue despite the absence of a rigid mechanical anchor to the skull. Our results indicate that such probes can leverage the properties of organic bioelectronics to enhance our understanding of neural network maturation in health and disease.

2. Results

We microfabricated a two-shank conformable implantable probe based on a parylene-C (Pa-C) substrate and PEDOT:PSS electrodes. The microelectrodes were 9×25 μm^2 with 25 μm inter-electrode spacing in a staggered format to ensure sufficient density for spike sorting while maintaining extended spatial coverage for LFP analysis (**Figure** 1A). The electrochemical impedance spectrum of these electrodes demonstrated low impedance ($\approx$15 KΩ ± 500 Ω at 1 kHz; Figure 1B), consistent with the known properties of conducting polymers.[49,50] Moreover, impedance values were consistent both within and across multiple devices, confirming the robustness of the fabrication process (Figure 1B, and Figure S1, Supporting Information). The tip of the probe contained a 30 μm diameter perforation accomplished by dry etching. This perforation accommodated a sharpened tungsten (W) microwire-based stylet used to insert the probe into the brain (Figure 1A,C). To improve the accessibility and versatility of the probe, we developed a simple electrochemical etching process that allows the sharpening of commercially available W-microwires into functional customized stylets (Figure 1C, Experimental Section). As a result, the probe and stylet combination can be easily modified to accommodate a variety of experimental set-ups and targets. Fabricated stylets were stereotactically coated with DiI (1,1′-dioctadecyl-3,3,3′,3′-tetramethylindocarbocyanine perchlorate), a lipophilic membrane stain, to allow post-mortem probe visualization. Probes were prepared and loaded onto stylets prior to the surgery (Figure 1D), enhancing the reliability and decreasing the duration of the implantation procedure. We implanted them in multiple brain areas with the aid of the stylet to facilitate stereotactic targeting (Figure 1E, and Video S1, Supporting Information). Upon reaching the desired stereotactic coordinates, the stylet was withdrawn, leaving only the conformable shank in contact with the tissue and no rigid structures on the skull (Figure 1E). With this approach, we were able to consistently implant conformable shanks into the brains of developing mouse pups. In contrast to rigid probes where increasing depth of implantation carries a higher risk of device failure, we were able to target desired structures at various depths below the cortical surface. We confirmed probe positions with immunohistochemistry and assessed tissue integrity along the probe tract compared to tissue at an adjacent unimplanted site (Figure 1F). We did not find a significant difference in cell density between
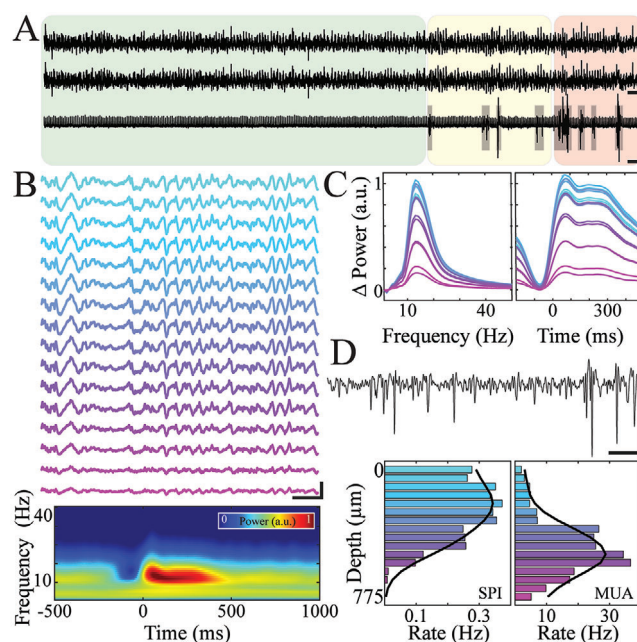

Figure 2. Electrophysiological recording and characterization of developing cortical layers using NeuroShank. A) Sample LFP recording from the neocortex of postnatal day 13 mouse pup (two channels, upper and middle; scale bar, 400 μV, 1 s) and corresponding nuchal EMG (bottom; scale bar, 2 mV, 1 s) demonstrating multiple brain states (green = quiet sleep; yellow = active sleep; red = wakefulness). B) Representative cortical LFP (1250 Hz) containing spindle oscillations (top; scale bar, 200 μV, 500 ms). Cool to warm colors represent superficial to deep electrode placement. Trigger-averaged time-frequency spectrogram of cortical LFP at the time of sleep spindles (bottom). C) Depth differentiation of spindle-aligned cortical neural activity power in frequency (left) and time (right). Cool to warm colors represent superficial to deep electrode placement. D) Sample high pass filtered (> 250 Hz) traces of cortical recording showing various amplitude action potentials (top; scale bar 10 ms, 40 μV). Distribution of spindle occurrence rate (left) and multi-unit firing rate across electrodes (right).

the tissue sites, suggesting minimal cell loss associated with implantation (Figure 1G,H). Thus, the combination of conformable probes and W-based stylet allows for facile and safe targeting of deep structures in developing brains without inducing significant cellular disruption.

Next, we investigated the electrophysiological data acquired by these probes. We first implanted NeuroShanks into the cortex of mouse pups (aged postnatal days 10–14) under isoflurane anesthesia. The simplicity of the implantation procedure enabled a brief duration of anesthesia. Mouse pups were concurrently monitored using electromyography (EMG) and electrocardiography (EKG) to determine when anesthetic recovery was complete. We then continuously recorded neural data from the mouse pups, capturing naturalistic sleep/wake transitions for up to 3 h post-implantation (**Figure** 2A). The acquired LFP had a well-defined spatial distribution across the channels of the probe linearly implanted across cortical layers, highlighting the lack of cross-talk between electrodes. The signal-to-noise ratio (SNR) of the recordings was sufficiently high to permit the automatic detection of thalamocortical sleep spindles (Figure 2B) that were characterized by 10–15 Hz peak frequency content (Figure 2C,D). We
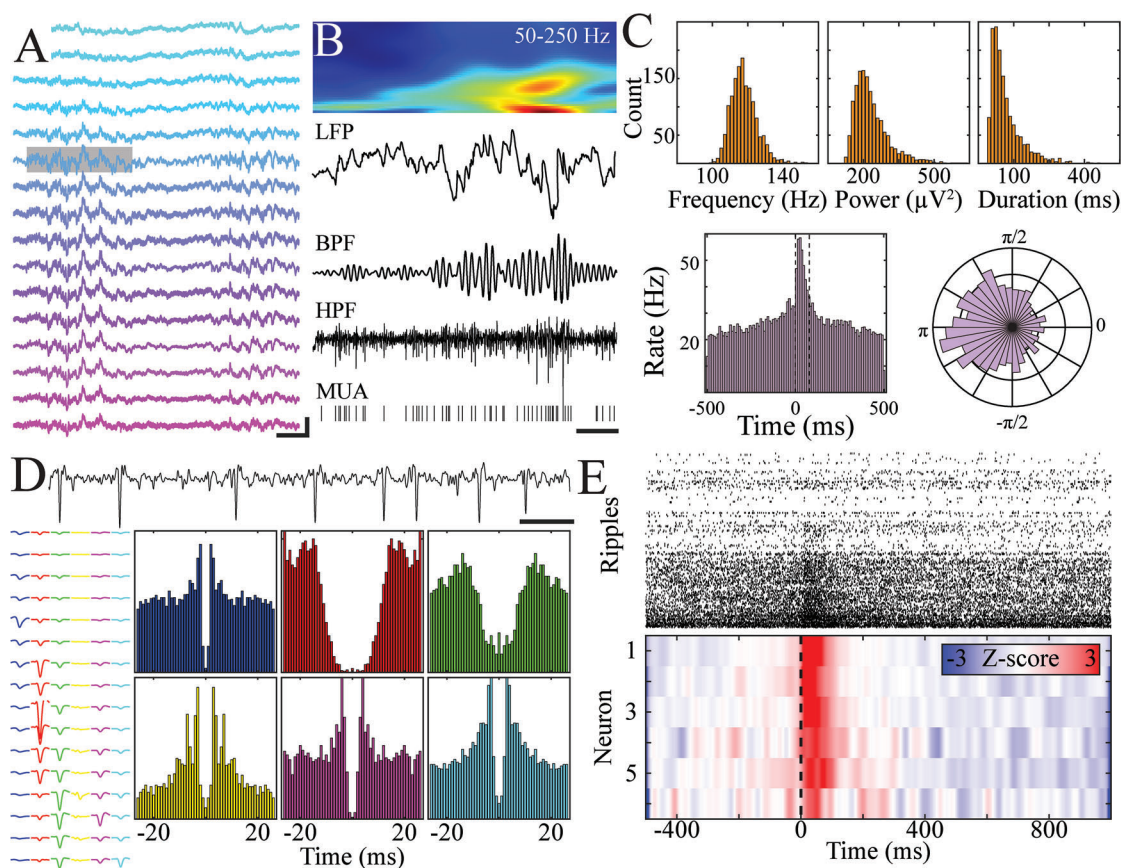
Figure 3. NeuroShank enables LFP and single unit recording in developing hippocampus. A) Representative hippocampal recording containing a sharp wave-ripple (shaded in gray; scale bar, 200 µV, 250 ms). Cool to warm colors represent superficial to deep electrode placement. B) Time-frequency spectrogram of a time epoch containing a sharp wave-ripple (LFP) with its corresponding band-pass filter (BPF), high-pass filter (HPF), and multi-unit raster (MUA). Scale bar, 50 ms. C) Frequency, power, and duration histograms of developmental ripples (top; orange). Multi-unit firing rate at the time of hippocampal ripples showing increased spiking at the time of ripple oscillations (bottom left). Phase-modulation of hippocampal spiking at the time of ripples highlighting phase preferences to the trough of the oscillation (bottom right). D) Sample high pass filtered trace of the developing hippocampus (postnatal day 16) showing action potentials of various amplitudes (top; scale bar, 40 µV, 10 ms). The average waveform of six putative single units showing variable localization across probe electrodes (left; 4 ms window) and their corresponding auto-correlograms (bottom right). E) Raster plot (top) and z-scored firing rates (bottom) of putative single unit firing during sharp wave ripples.

found that the power of these oscillations was maximal in the mid to superficial cortical layers (Figure 2C,D). We then high-pass filtered the data and identified neural spiking activity, validating the ability of the probes to acquire high spatiotemporal resolution patterns (Figure 2D, upper). An increase in neural spiking was observed at the time of detected spindle oscillations, confirming their physiologic nature (Figure 2D, and Figures S2 and S3, Supporting Information). Spikes were detected across all channels of the probes, establishing a profile of the population's instantaneous firing rate across cortical layers (Figure 2D).

We then aimed to test the ability of the probes to acquire neural data from deeper brain regions. We targeted the hippocampus (P12-16), and the linear layout of the probe permitted differentiation of its known layered structure (**Figure 3A**). Furthermore, we were able to detect hippocampal ripples, which are brief, high-frequency oscillations critical for memory that emerge during the third postnatal week of rodent development (Figure 3B). These ripples were accompanied by a time-locked and phase-locked in-

crease in neural spiking activity, consistent with their role in organizing action potentials (Figure 3C). Individual action potentials were detectable with resolution sufficient to permit template-based clustering into putative single unit activity (Figure 3D, and Figures S4 and S6, Supporting Information). Similar single-unit quality was also achieved for cortical cells (Figures S2 and S5, Supporting Information). These single units were observed across multiple channels of the probe, facilitating the clustering process and enabling classification based on firing rate during epochs of population activity (Figure 3E).

After establishing the ability of NeuroShanks to acquire both high spatiotemporal resolution LFP and single-unit activity from the mouse pup brain, we aimed to evaluate their recording stability. The stability of the neural activity patterns is of particular importance because the probes lack skull-based rigid anchoring components and the high-water content of the immature brain predisposes to probe movement. We employed a two-pronged approach, focusing first on LFP and then on neural spiking
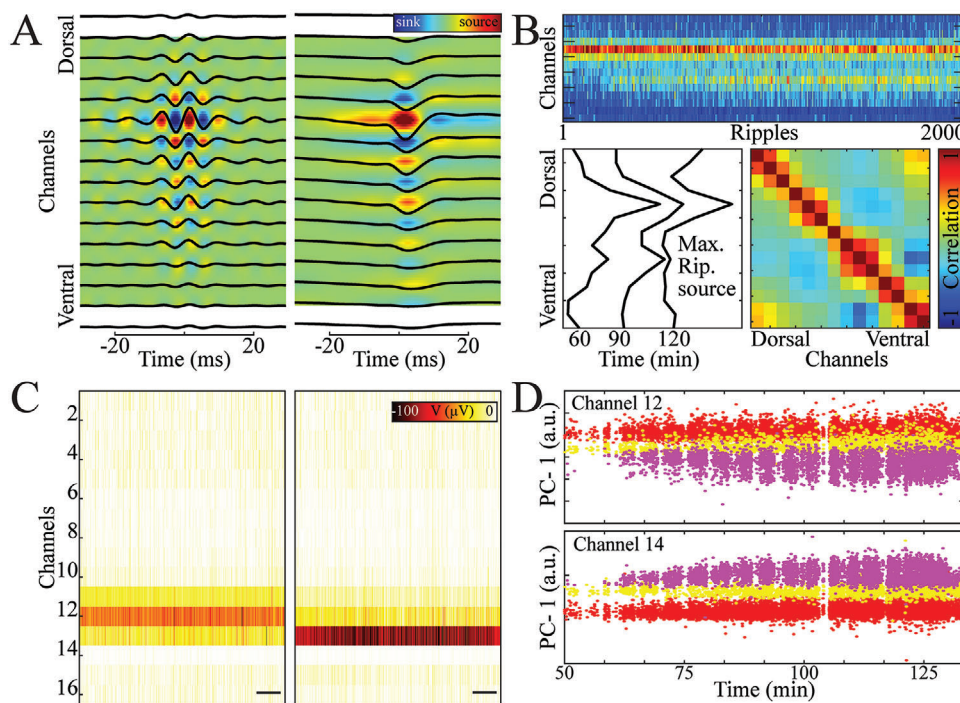
**ADVANCED
SCIENCE NEWS**

www.advancedsciencenews.com

**ADVANCED
HEALTHCARE
MATERIALS**

www.advhealthmat.de

Figure 4. NeuroShank enables stable electrophysiological recording at LFP and action potential resolution without mechanical anchoring. A) Average current-source density (CSD) of hippocampal sharp wave-ripples (left: Ripple component; right: Sharp wave component). B) Source localization of hippocampal sharp wave ripples across channels over the course of recording (warm colors represent maximal source localization; top). Sample source localization of sharp wave ripples at 30-min intervals (bottom left). Pair-wise correlation matrix of the source localization between channels highlighting a stable source (bottom right). C) Heatmaps of two cortical single unit spiking amplitudes demonstrating stable localization over the course of recording (scale bar, 2000 spikes [left], 500 spikes [right]). D) First principal components of two channels for three cortical single units demonstrating stability over the course of recording.

features. Current source density (CSD) analysis enabled localization of the source/sink distribution of ripple oscillations across the hippocampal layers (**Figure 4**A). Quantification of the position of the maximal oscillation source/sink over the duration of the recording period revealed a static peak, consistent with a stable probe position relative to brain tissue (Figure 4B). This was further validated using frequency co-modulation (Figure S7, Supporting Information). The amplitude of single unit action potential waveforms across the recording remained steady across multiple channels during the recording (Figure 4C), and principal components of these waveforms were also uniformly distributed over time (Figure 4D). Taken together, these results suggest that the conformable probes are capable of maintaining a precise, stable position when implanted into immature brain tissue.

3. Conclusion

We demonstrated the applicability and versatility of conformable conducting polymer-based implantable neural interface devices (NeuroShanks) to stably acquire high-quality neural data from the developing brain. The unique properties of these devices enabled compatibility with short-duration surgery required in immature organisms and natural sleep and wake post-implantation. Furthermore, we showed that such devices can be easily targeted to brain regions using an easy-to-fabricate and removable

tungsten stylet, resulting in an implantation approach that minimizes disruption of fragile immature tissue despite use in an unanesthetized preparation. We were able to detect and characterize oscillatory patterns in the LFP of the cortex and hippocampus, as well as identify neural spiking from individual neurons. Critically, the recordings were stable over time, enabling tracking of activity from microcircuits and neurons across behavioral states.

These results reveal the potential for conformable and organic devices to enhance the ability to monitor neural circuits as they mature, providing the means to investigate key questions in developmental neuroscience in animal models. Although the current approach still necessitates acute recording (several hours' duration) due to the inability to fully implant all recording and data transmission components within the animal, the minimally invasive surgery and lack of skull-based fixation make a critical step toward capacity for chronic recording. Future integration with soft electronics capable of data processing and non-invasive data transmission methods[29,51,52] could realize such longitudinal recording in mice as they develop from the early postnatal period into adulthood. Furthermore, the quality and resolution of signals obtained suggest that such approaches are translatable to pediatric patients who require clinical neurophysiologic studies, allowing increased information to be derived without introducing additional risks associated with device implantation.

2304164 (5 of 8)

4. Experimental Section

Materials:

Material	Source
PEDOT:PSS (Clevios PH1000)	Heraeus
(3-Glycidyloxypropyl) trimethoxysilane (GOPS)	Sigma-Aldrich
4-dodecyl benzene sulfonic acid (DBSA)	
3-(trimethoxysilyl) propyl methacrylate (A-174 silane)	
Phosphate buffered saline (PBS) tablets	
Micro 90 concentrated cleaning solution	Special Coating Services
AZnLOF2020 (negative photoresist)	MicroChemicals, Merck
AZ9260 (positive photoresist)	
AZ 400 K developer	
AZ 300 MIF developer	
Tungsten 99.95% CS wire (50 µm in diameter)	California Fine Wire Company
Electronic components	Digi-key
Printed circuit board (PCB) circuits	Eurocircuits

Probe Fabrication: Implantable NeuroShanks were fabricated on single-side polished Si wafers (100 mm outer diameter, 550 µm thickness). A parylene C layer (1.5 µm thickness) was coated using SCS Labcoater 2. Metal lift-off first involved spin-coating negative photoresist and baking at 105 °C for 90 s. This was followed by UV exposure with a Suss MA6 Mask Aligner and developed with AZ 300MIF. Angstrom EvoVac Multi-Process was used to deposit a Ti adhesion layer (10 nm in thickness) and a subsequent Au layer (150 nm in thickness) before patterning with photoresist remover. Another layer of parylene C (1.5 µm in thickness) for insulation was deposited, and its adhesion to the bottom layer was enhanced during chemical vapor deposition with A-174 silane. A third layer of parylene C (1.5 µm in thickness) for sacrificial peel-off was deposited, and its adhesion to the second layer was reduced with spin-coating 0.5 v/v% Micro-90 diluted in deionized water. Then, a layer of AZ9260-positive photoresist was spin-coated at 5000 rpm, baked at 115 °C for 90 s, exposed using a Suss MA6 Mask Aligner, and developed with AZ400K developer (1:4 with deionized water) to pattern the stacked layers. A plasma reactive ion-etching (RIE) process (Oxford Plasmalab 80; 180 W, 50 sccm O2, and 2 sccm SF6) etched the layers to shape electrodes and contact pads. An extra layer of AZnLOF2020 was spin-coated at 3000 rpm between the silane-treated parylene C and the metal layer for clean etching. The perimeter of each contact pad was etched, and the remaining parylene C on the photoresist was removed when bathed in acetone. Next, high-conductivity PEDOT:PSS (80% PEDOT:PSS, 20% ethylene glycol, 0.6% DBSA, all v/v) was spin-coated on electrodes, and the sacrificial parylene C layer was peeled off for patterning. Finally, the wafer was thoroughly cleaned with acetone and isopropyl alcohol (IPA) and released in a bath of deionized water. Mixed-conducting particulate composites[52] were used to connect soft NeuroShanks with rigid PCB boards containing preamplification circuitry.

Stylet Fabrication: Custom stylets were fabricated as shuttles to penetrate brain tissue and carry NeuroShanks to the targeted brain region. A surgical blade was used to strip 4 mm of insulation coating off each end of tungsten wires. Each stripped wire was fixed onto metal bars using glue and tape, with one end soldered and the other end a stylet tip. An electrochemical etching process was used to sharpen stylet tips. The soldered end was connected to the anode of a waveform generator and the cathode was connected to a stainless-steel sheet (1 cm). Portions of the tip and sheet were submerged in a NaOH (1 mM) solution. DC voltage (+6 V) was applied for 20 s to ensure thorough etching of the stylet tip to a cone shape at the solution surface. Etched stylets were imaged and measured using a microscope. Prior to surgical implantation, fabricated stylets were stereotactically lowered 100 µm from the tip into DiI and held for 30 s for coating. Sharp stylet tips were then threaded through anchor holes of implantable shanks, such that the soft shank would move only into the brain with the stylet but not out when retracting the stylet.

Surgical Protocol: All animal experiments were performed in accordance with protocols approved by the Institutional Animal Care and Use Committee at Columbia University Irving Medical Center (Protocol AC-AABI5568, Investigator Jennifer N. Gelinas MD, PhD). Swiss–Webster mouse pups (5-10 g, 10–16 days of age, both sexes) received intracranial implantation and neurophysiologic recording. Anesthesia was induced with 3% isoflurane and maintained with 1-1.5% isoflurane. Time under anesthesia was minimized (< 60 min) for expedited postoperative recovery. Ketoprofen and bupivacaine analgesia were administered. Fine gauge wire electrodes served as electromyography (EMG) and EKG probes and were placed subcutaneously in the chest and nuchal areas for online monitoring of respiration, heart rate, and muscle tone. Pups were comfortably placed on a customized platform. A small cranial burr hole was opened over the cerebellum for the reference electrode. Small cranial windows or burr holes (centered at AP 1.5–2 mm, ML 1–1.5 mm, sized proportional to age) were opened for implantation of NeuroShanks. After implantation, the cranial window was covered with a small piece of Gelfoam. Pups were transferred into a custom chamber for recovery and recording.

Probe Insertion and Implantations: The assembled NeuroShank-stylet-board complex was held above the brain by a micro-manipulator (Thor-Labs). Stylet-mounted NeuroShanks were stereotactically advanced to targeted depth. Drops of saline were applied to the cranial window to assist in the positioning of the unimplanted portion of the soft device. With the electrodes conforming to the target tissue, the stylet was stereotactically retracted out of the brain. The flexible ribbon of the NeuroShank connected to the preamplifier board, which was suspended above the animal. Lastly, the stylet was removed from the preamplifier board to complete implantation.

Electrophysiological Recordings: Electrophysiological signal acquisition was performed in a custom-built chamber grounded to shield ambient electrical noise. The chamber provided optimal temperature and humidity as well as olfactory cues familiar to mouse pups. Heart rate steadily increased before plateauing and normal sleep-wave cycles resumed, indicating recovery from anesthesia. Preamplifier and acquisition circuitry (RHD2000 Intan Technology) were used to amplify, digitize, and store signals at 2000 Hz with a 16-bit format. Spontaneous activity was acquired for up to 3 h.

Perfusion and Histology: Mouse pups were euthanized with intraperitoneal injection of pentobarbital (100 mg kg^{-1}) after recording. Pups were then perfused with PBS and 4% paraformaldehyde (PFA). Extracted brains were kept in 4% PFA for 24 h for fixation prior to transfer to PBS solution. Brains were sliced either coronally using a Leica vibratome vt1000s at 60 µm thickness. Slices were first incubated for 1 h at room temperature in a blocking solution (PBS (0.01 M), 3% normal donkey serum, and 0.3% Triton X-100). Slices were then incubated for at least 12 h in a solution containing anti-vesicular glutamate transporter 2 (VGlut2) polyclonal guinea-pig antibody (AB2251-I Sigma Millipore) in a 1:1000 dilution at 4 °C. Subsequently, slices were incubated for 2 h in a solution of secondary antibody (Alexa Fluor 594 AffiniPure Donkey Anti-guinea pig IgG (H+L) 706-585-148), Jackson Immunoresearch) at 1:500 dilution at room temperature. Next, slices were incubated for 5 min with DAPI (D9542-5MG; Sigma-Aldrich) at 1:10 000 dilution at room temperature. Finally, slices were mounted with Fluoromount-G (00-4958-02, ThermoFisher). An ECHO Revolve microscope was used to capture fluorescent images of mounted brain slices. Cell density quantification was done using ImageJ. Intensity and threshold levels were kept constant for all images.

Sleep Scoring and Local Field Potential Analysis: NeuroShank recordings were visually inspected with Neuroscope (https://neurosuite.sourceforge.net). All data was processed and analyzed with MATLAB (MathWorks). Raw recordings were resampled from 20 000 to 1250 Hz to highlight local field potentials (LFP). EKG and EMG signals were

**ADVANCED
SCIENCE NEWS**

www.advancedsciencenews.com

**ADVANCED
HEALTHCARE
MATERIALS**

www.advhealthmat.de

separated by detecting EKG peaks. EMG power envelope was obtained through high-pass filtering at 300 Hz, full-wave rectification, and Gaussian smoothing. Epochs when EMG power exceeding a threshold of 1.5—2.5 standard deviations above mean, were detected and consistent with high muscle tone. Detected epochs were visually inspected for accuracy. Epochs lasting at least 1.5 s were classified as wakefulness. Epochs less than 1.5 s were classified as myoclonic twitches. An epoch of muscle atonia consistent with sleep was detected when EMG power did not exceed the threshold for at least 2 s. Putative active and quiet sleep epochs were further delineated. Epochs spanning 1 s before and 4 s after each twitch were classified as active sleep. Epochs of muscle atonia with behavioral quiescence for at least 10 consecutive seconds were classified as quiet sleep.

Electrophysiological Event Detection: Cortical spindle oscillations were detected from all channels in animals with NeuroShanks implanted in the primary somatosensory cortex. LFP was first band-pass filtered at 10–20 Hz, and the absolute value of the Hilbert transform was obtained for quiet sleep epochs. Two thresholds were calculated based on the SD of all channels, with the soft threshold 2 times the SD and the hard threshold 2.5 times the SD. First, epochs exceeding the soft threshold were detected as events. Second, events 100 ms apart were merged. Then, only events that continuously exceeded the hard threshold for 50 ms were kept. Finally, events shorter than 200 ms or longer than 2 s were excluded.

Sharp-wave ripples were detected from channels at the pyramidal layer from animals with NeuroShanks implanted in the hippocampus, using the above-described LFP filter-thresholding method in quiet sleep epochs. The band-pass filter was 100–200 Hz. Soft and hard thresholds were two and four times, respectively, the SD of the pyramidal layer channels. The merging duration was 10 ms. The minimum hard threshold duration was 10 ms. The minimum and maximum durations were 30 ms and 1 s, respectively.

Extracellular neural spiking was detected from each channel in all animals. Raw recordings were high-pass filtered at 250 Hz. For each animal, the 10 longest quiet sleep epochs were taken, and for each channel, the noise floor was calculated. Negative peaks greater than four times this noise floor were detected as spikes. Coincidental spikes across more than eight consecutive channels were deemed artifactual and removed from downstream analyses. The occurrence rate of oscillations and neural spiking were calculated as number of events divided by the total duration of quiet sleep epochs.

Time-Frequency Power and Current-Source Density Analysis: Analytic Gabor wavelet transform was used to obtain time-frequency spectrograms of neural oscillations. Spindle trigger-averaged spectrograms were aligned at spindle starts and normalized by the number of spindles. Spectral power change across channels was calculated as the difference between peak- and pre-spindle power. Temporal power change across channels was calculated as the difference between the spindle band and other frequencies. Current-source density was calculated using the second spatial derivative of LFP, with average ripple CSD calculated using 100–150 Hz filtered LFP and average sharp wave CSD calculated using wideband LFP.

Peri-Ripple Time Histogram and Firing Phase: Peri-ripple time histograms were calculated by binning and averaging unit firing during ripple events, aligned at ripple starts. The firing phase polar histogram was obtained by binning the unwrapped ripple phases at which spiking occurs.

Single Unit Clustering and Analysis: Detected multi-unit activity clustered using KiloSort and visualized using Phy2. No manual curation of clusters was performed. Auto-correlograms and cross-correlograms were obtained from the temporal convolution of single-unit spike trains. Single-unit clustering in principal component spaces and stability over time were visualized using principle component weights calculated by KiloSort.

Statistical Analysis: All statistical analyses were performed using MATLAB. Group differences were assessed with two-sided paired t-tests ($\alpha = 0.05$) with at least three replicates. Data was presented as mean $\pm$ SEM.

Supporting Information

Supporting Information is available from the Wiley Online Library or from the author.

Conflict of Interest

The authors declare no conflict of interest.

Author Contributions

J.N.G., D.K., and L.M. conceived the project. L.M., D.J.W., and D.K. designed, developed, fabricated, and characterized materials and devices. L.M., D.K., and J.N.G. performed the electrophysiology in vivo rodent experiments and analysis. All authors contributed to writing the paper.

Data Availability Statement

The data that support the findings of this study are available from the corresponding author upon reasonable request.

[1] M. Le Van Quyen, I. Khalilov, Y. Ben-Ari, *Trends Neurosci.* **2006**, *29*, 419.

[2] R. Cossart, R. Khazipov, *Physiol. Rev.* **2022**, *102*, 343.

[3] P. Jastrzebska-Perfect, S. Chowdhury, G. D. Spyropoulos, Z. Zhao, C. Cea, J. N. Gelinas, D. Khodagholy, *Adv. Funct. Mater.* **2020**, *30*, 1909165.

[4] D. Khodagholy, J. J. Ferrero, J. Park, Z. Zhao, J. N. Gelinas, *Trends Neurosci.* **2022**, *45*, 968.

[5] G. Buzsáki, E. Stark, A. Berényi, D. Khodagholy, D. R. Kipke, E. Yoon, K. D. Wise, *Neuron* **2015**, *86*, 92.

[6] P. Dahal, O. J. Rauhala, D. Khodagholy, J. N. Gelinas, *Proc. Natl. Acad. Sci. U. S. A.* **2023**, *120*, 2207909120.

[7] P. Dahal, N. Ghani, A. Flinker, P. Dugan, D. Friedman, W. Doyle, O. Devinsky, D. Khodagholy, J. N. Gelinas, *Brain* **2020**, *143*, 28.

[8] A. R. Hassan, Z. Zhao, J. J. Ferrero, C. Cea, P. Jastrzebska-Perfect, J. Myers, P. Asman, N. F. Ince, G. McKhann, A. Viswanathan, S. A. Sheth, D. Khodagholy, J. N. Gelinas, *Adv. Sci.* **2022**, *9*, 2202306.

[9] A. P. Alivisatos, M. Chun, G. M. Church, K. Deisseroth, J. P. Donoghue, R. J. Greenspan, P. L. McEuen, M. L. Roukes, T. J. Sejnowski, P. S. Weiss, R. Yuste, *Science* **2013**, *339*, 1284.

[10] G. Buzsáki, N. Logothetis, W. Singer, *Neuron* **2013**, *80*, 751.

[11] M. A. L. Nicolelis, E. E. Fanselow, A. A. Ghazanfar, A. Donald, T. Organization, *Neuron* **1997**, *19*, 219.

[12] M. A. Wilson, B. L. McNaughton, *Science* **1993**, *261*, 1055.

[13] S. M. Wellman, J. R. Eles, K. A. Ludwig, J. P. Seymour, N. J. Michelson, W. E. McFadden, A. L. Vazquez, T. D. Y. Kozai, *Adv. Funct. Mater.* **2018**, *28*, 1701269.

[14] G. Buzsáki, *Nat. Neurosci.* **2004**, *7*, 446.

[15] J. J. Jun, N. A. Steinmetz, J. H. Siegle, D. J. Denman, M. Bauza, B. Barbarits, A. K. Lee, C. A. Anastassiou, A. Andrei, Ç. Aydın, M. Barbic, T. J. Blanche, V. Bonin, J. Couto, B. Dutta, S. L. Gratiy, D. A. Gutnisky, M. Häusser, B. Karsh, P. Ledochowitsch, C. M. Lopez, C. Mitelut, S. Musa, M. Okun, M. Pachitariu, J. Putzeys, P. D. Rich, C. Rossant, W. Sun, K. Svoboda, et al., *Nature* **2017**, *551*, 232.

[16] R. a Normann, E. M. Maynard, P. J. Rousche, D. J. Warren, *Vision Res.* **1999**, *39*, 2577.

[17] M. Minlebaev, M. Colonnese, T. Tsintsadze, A. Sirota, R. Khazipov, *Science* **2011**, *334*, 226.

[18] J. W. Jeong, G. Shin, S. Il Park, K. J. Yu, L. Xu, J. A. Rogers, *Neuron* **2015**, *86*, 175.

[19] L. Luan, X. Wei, Z. Zhao, J. J. Siegel, O. Potnis, C. A. Tuppen, S. Lin, S. Kazmi, R. A. Fowler, S. Holloway, A. K. Dunn, R. A. Chitwood, C. Xie, *Sci. Adv.* **2017**, *3*, 1601966.

[20] A. Y. Rwei, W. Lu, C. Wu, K. Human, E. Suen, D. Franklin, M. Fabiani, G. Gratton, Z. Xie, Y. Deng, S. S. Kwak, L. Li, C. Gu, A. Liu, C. M. Rand, T. M. Stewart, Y. Huang, D. E. Weese-Mayer, J. A. Rogers, *Proc. Natl. Acad. Sci. U. S. A.* **2020**, *117*, 31674.

[21] Y. Liu, J. Li, S. Song, J. Kang, Y. Tsao, S. Chen, V. Mottini, K. McConnell, W. Xu, Y. Q. Zheng, J. B. H. Tok, P. M. George, Z. Bao, *Nat. Biotechnol.* **2020**, *38*, 1031.

[22] L. Luan, R. Yin, H. Zhu, C. Xie, *Ann. Rev. Biomed. Eng.* **2023**, *25*, 185.

[23] Z. Zhao, H. Zhu, X. Li, L. Sun, F. He, J. E. Chung, D. F. Liu, L. Frank, L. Luan, C. Xie, *Nat. Biomed. Eng.* **2022**, *7*, 520.

[24] S. Zhao, X. Tang, W. Tian, S. Partarrieu, R. Liu, H. Shen, J. Lee, S. Guo, Z. Lin, J. Liu, *Nat. Neurosci.* **2023**, *26*, 696.

[25] R. Lycke, R. Kim, P. Zolotavin, J. Montes, Y. Sun, A. Koszeghy, E. Altun, B. Noble, R. Yin, F. He, N. Totah, C. Xie, L. Luan, *Cell Rep.* **2023**, *42*, 112554.

[26] Z. Zhao, C. Cea, J. N. Gelinas, D. Khodagholy, *Proc. Natl. Acad. Sci. U. S. A.* **2021**, *118*, 2022659118.

[27] Z. Zhao, G. D. Spyropoulos, C. Cea, J. N. Gelinas, D. Khodagholy, *Sci. Adv.* **2022**, *8*, abm7851.

[28] C. Cea, Z. Zhao, D. J. Wisniewski, G. D. Spyropoulos, A. Polyravas, J. N. Gelinas, D. Khodagholy, *Nat. Mater.* **2023**, *22*, 1227.

[29] C. Cea, G. D. Spyropoulos, P. Jastrzebska-Perfect, J. J. Ferrero, J. N. Gelinas, D. Khodagholy, *Nat. Mater.* **2020**, *19*, 679.

[30] K. Tybrandt, D. Khodagholy, B. Dielacher, F. Stauffer, A. F. Renz, G. Buzsáki, J. Vörös, *Adv. Mater.* **2018**, *30*, 1706520.

[31] G. D. Spyropoulos, J. Savarin, E. F. Gomez, D. T. Simon, M. Berggren, J. N. Gelinas, E. Stavrinidou, D. Khodagholy, *Adv. Mater. Technol.* **2020**, *5*, 11900652.

[32] T. Suzuki, K. Mabuchi, S. Takeuchi, presented at 1st Int. IEEE/EMBS Conf. on Neural Engineering (NER) Capri, Italy, March **2003**.

[33] S. Takeuchi, D. Ziegler, Y. Yoshida, K. Mabuchi, T. Suzuki, *Lab Chip* **2005**, *5*, 519.

[34] K. Srikantharajah, R. Medinaceli Quintela, K. Doerenkamp, B. M. Kampa, S. Musall, M. Rothermel, A. Offenhäusser, *Sci. Rep.* **2021**, *11*, 18920.

[35] M. Wang, Y. Zhang, P. Xue, Y. Zhou, W. Shi, S. Zhou, Y. Wang, H. Li, R. Zhao, *Seizure* **2021**, *86*, 102.

[36] A. Hyslop, S. Wang, J. P. Bryant, S. Bhatia, C. Sandoval-Garcia, K. Karkare, J. Ragheb, *Epilepsy Res.* **2021**, *177*, 106765.

[37] A. S. Levy, L. L. Bystrom, E. C. Brown, M. Fajardo, S. Wang, *Clin. Neurol. Neurosurg.* **2023**, *234*, 108012.

[38] S. Domínguez, L. Ma, H. Yu, G. Pouchelon, C. Mayer, G. D. Spyropoulos, C. Cea, G. Buzsáki, G. Fishell, D. Khodagholy, J. N. Gelinas, *Elife* **2021**, *10*, 69011.

[39] J. Shen, M. T. Colonnese, *J. Neurosci.* **2016**, *36*, 12259.

[40] H. Yu, W. Kim, D. K. Park, J. H. Phi, B. C. Lim, J.-H. Chae, S.-K. Kim, K. J. Kim, F. A. Provenzano, D. Khodagholy, J. N. Gelinas, *Epilepsia* **2024**, *65*, 190.

[41] O. J. Rauhala, S. Dominguez, G. D. Spyropoulos, J. J. Ferrero, T. R. Boyers, P. Jastrzebska-Perfect, C. Cea, D. Khodagholy, J. N. Gelinas, *Adv. Mater. Technol.* **2020**, *5*, 1900663.

[42] M. R. Abidian, D. C. Martin, *Biomaterials* **2008**, *29*, 1273.

[43] X. Cui, D. C. Martin, *Sens. Actuators., B* **2003**, *89*, 92.

[44] A. R. Hassan, Z. Zhao, J. J. Ferrero, C. Cea, P. Jastrzebska-Perfect, J. Myers, P. Asman, N. F. Ince, G. McKhann, A. Viswanathan, S. A. Sheth, D. Khodagholy, J. N. Gelinas, *Adv. Sci.* **2022**, *9*, 2202306.

[45] D. Khodagholy, J. N. Gelinas, G. Buzsáki, *Science* **2017**, *358*, 369.

[46] D. Khodagholy, J. N. Gelinas, T. Thesen, W. Doyle, O. Devinsky, G. G. Malliaras, G. Buzsaki, *Nat Neurosci.* **2015**, *18*, 310.

[47] D. R. Yao, H. Yu, O. J. Rauhala, C. Cea, Z. Zhao, J. N. Gelinas, D. Khodagholy, *Adv. Sci.* **2022**, *9*, 2104404.

[48] P. Jastrzebska-Perfect, G. D. Spyropoulos, C. Cea, Z. Zhao, O. J. Rauhala, A. Viswanathan, S. A. Sheth, J. N. Gelinas, D. Khodagholy, *Sci. Adv.* **2020**, *6*, aaz6767.

[49] R. Green, M. R. Abidian, *Adv. Mater.* **2015**, *27*, 7620.

[50] D. A. Koutsouras, P. Gkoupidenis, C. Stolz, V. Subramanian, G. G. Malliaras, D. C. Martin, *ChemElectroChem* **2017**, *4*, 2321.

[51] Z. Zhao, G. D. Spyropoulos, C. Cea, J. N. Gelinas, D. Khodagholy, *Sci. Adv.* **2022**, *8*, 7851.

[52] P. Jastrzebska-Perfect, G. D. Spyropoulos, C. Cea, Z. Zhao, O. J. Rauhala, A. Viswanathan, S. A. Sheth, J. N. Gelinas, D. Khodagholy, *Sci. Adv.* **2020**, *6*, aaz6767.